GEOPHYSICAL RESEARCH LETTERS, VOL. 27, NO. 9, PAGES 1283-1286, MAY 1, 2000

Global Patterns of ENSO-induced Precipitation

Aiguo Dai and T. M. L. Wigley

National Center for Atmospheric Research, Boulder, Colorado

Abstract. Although there have been many analyses of El Niño/Southern Oscillation (ENSO) induced precipitation anomalies, global patterns from these analyses remain incomplete. Here we combine recent satellite estimates of oceanic precipitation and historical rain-gauge records to derive a global climatology of ENSO-induced precipitation anomalies using empirical orthogonal function (EOF) analyses. The patterns suggest that the re-arrangement of convection centers of the Walker circulation during ENSO events induces large precipitation anomalies in the tropics, while associated changes in the monsoon systems (through the Hadley cell) over the Pacific, Indian and Atlantic Oceans, and their interactions with midlatitude westerlies generate coherent anomaly patterns over the extratropics. Our results can be used to evaluate climate models and forecast ENSO-induced precipitation anomalies.

1. Introduction

ENSO is the single most important determinant of variability in global precipitation fields (*Dai et al.*, 1997). ENSO-induced precipitation anomalies over various regions have been documented through analyses of rain-gauge records from land stations [e.g., *Ropelewski and Halpert*, 1987, 1989; *Kiladis and Diaz*, 1989; *Shabbar et al.*, 1997; *Dai et al.*, 1997]. The anomaly patterns identified by these studies, however, are incomplete over the oceans and discontinuous over coastal regions, a disadvantage for global pattern analyses and for uses in climate model evaluations (*Dai et al.*, 2000).

Xie and Arkin (1997, henceforth X-A) merged rain-gauge records, satellite estimates, and reanalysis model output to derive global maps of monthly precipitation since 1979. Based on 1979-95 data, X-A presented global maps of composite precipitation differences between warm and cold ENSO episodes. Their maps, however, do not show many of the well-documented ENSO precipitation anomalies, especially over land areas (e.g., the western United States and Australia). This is partly because the composite method examines absolute precipitation anomalies. This fails to isolate the signal from local noise when short records are used and the signal is relatively weak (e.g., over extratropics).

Using a quality-controlled monthly precipitation data set for 1900-88 and EOF analyses, *Dai et al.* (1997) obtained a robust ENSO mode in global land precipitation fields. Here we extend this analysis to cover oceanic areas by including X-A data (updated to 1998). ENSO EOF modes are derived from the combined data set for seasonal and annual precipitation. Besides providing a more complete global picture of ENSO precipitation anomalies than any earlier analyses, these EOF maps also show many new features that have not been revealed before.

Paper number 1999GL011140.
0094-8276/00/1999GL011140$05.00

2. Data and Analysis Method

Monthly precipitation anomaly data on a 2.5° x 2.5° grid for 1900-78 were obtained from *Dai et al.* (1997), which were based on records from ~5300 stations over the continents and many islands. The gridded data agree well with other independently-derived data sets (e.g., *New et al.*, 1999), except for the periods before 1915 and after 1980 during which coverage was poor in *Dai et al.* (1997).

To maximize spatial and temporal coverage, we combined the monthly anomalies for 1979-98 from X-A with 1900-78 data from *Dai et al.* (1997). X-A anomalies are with respect to 1979-98, while Dai et al. anomalies are with respect to 1950-79. Both data sets have data over land for 1979-88; anomaly patterns over this period are comparable. The homogeneity of the combined data set is also confirmed from our EOF analysis: we did not find any discontinuity modes (which would be independent of and thus be separated from the ENSO modes). Therefore, we believe that the ENSO EOFs are not affected by the merging technique. The time series of seasonal and annual precipitation anomalies were normalized by their standard deviations at each grid box before being subjected to a standard EOF analysis. Note that the oceanic EOF patterns are derived from a much shorter record (1979-98) than over land where the record length varies from ~50 to 99 years. The analysis covers the domain from 60°S to 75°N.

3. Results

Fig. 1a shows that the amplitude of the first EOF of annual precipitation is correlated (r=0.76) with Darwin sea level pressure (SLP) (r=-0.76 with the Southern Oscillation Index) when the SLP data lead by two months (r=0.71 for zero lag). The EOF patterns (Figs. 1b & c) identify the main regions where precipitation is known to be strongly affected by ENSO, such as the equatorial Pacific and Indonesia-Australia region. In contrast to earlier land-based studies, however, Figs. 1b and 1c present a complete picture with continuous patterns of ENSO precipitation anomalies over the globe.

One of the main patterns not well documented in previous analyses is the propagation of large anomalies (dry during El Niños) over the eastern tropical Indian Ocean and Indonesia region northeastward into the North Pacific and southeastward into the South Pacific (across Australia) separated by wet anomalies over the equatorial Pacific. The *relative* ENSO signal (Fig. 1b) over these two paths is as strong as that over the Indonesia region, although the *absolute* precipitation anomalies (Fig. 1c) are much larger in the tropics

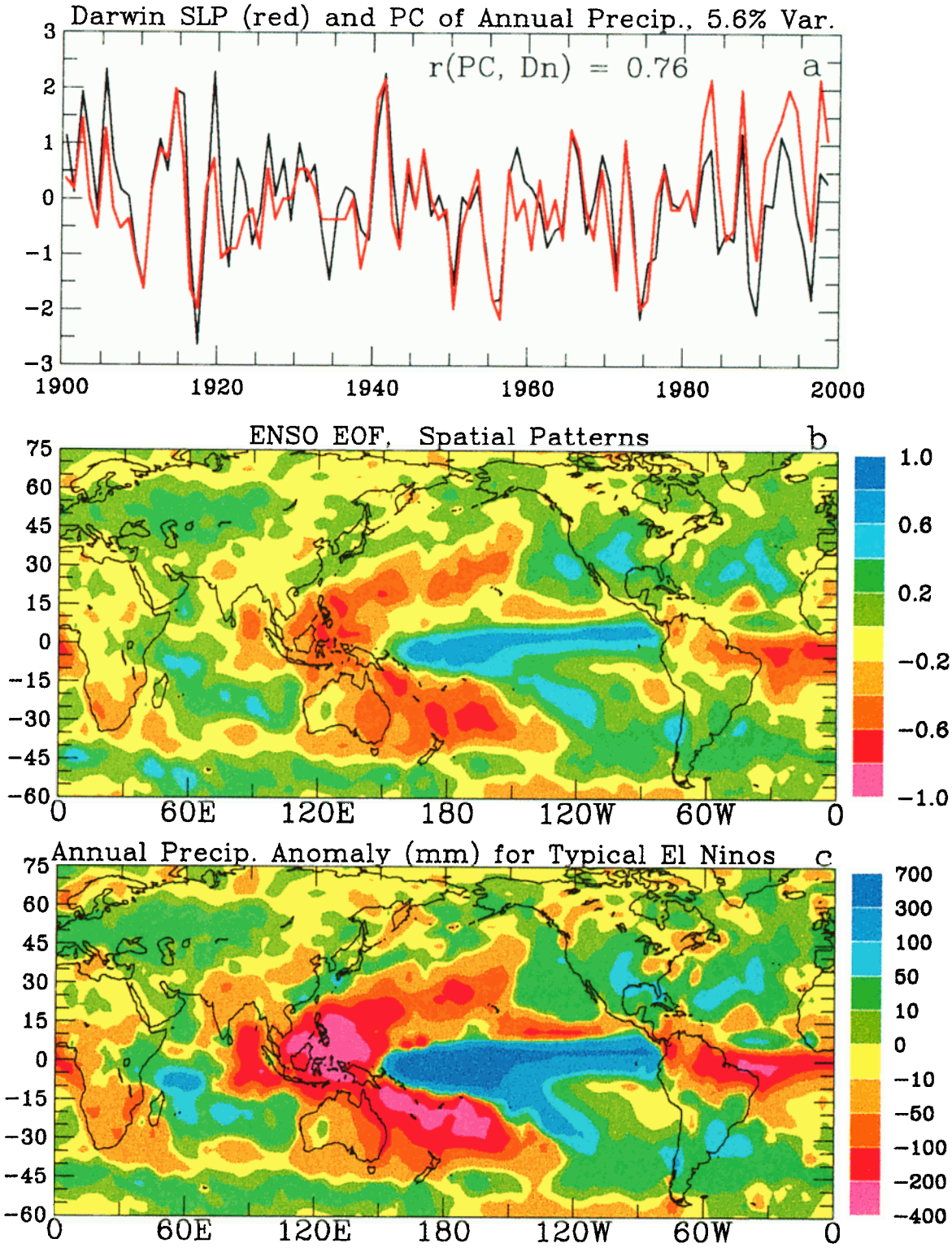

Figure 1. a: EOF 1 amplitudes (black line) for annual precipitation compared with normalized Darwin sea level pressure (red line) through 1998. Year n is plotted as n+0.5. b: EOF 1 pattern normalized to represent the grid-box correlation between the amplitude and annual precipitation. c: annual precipitation anomalies (mm) associated with a +1.0 anomaly in the EOF 1 time series (i.e, ~1.5 standard deviations for annual Darwin SLP). Note that yellow and light-green colors indicate statistically insignificant values.

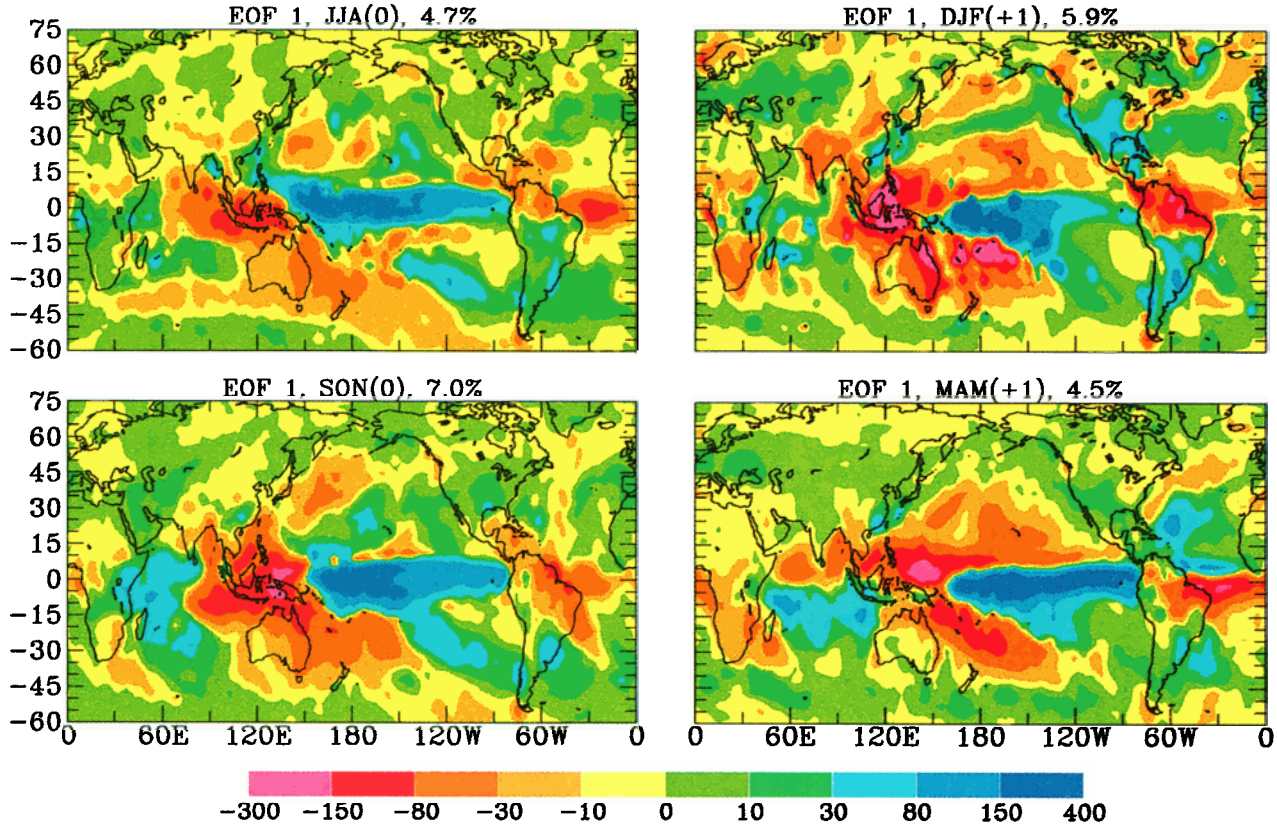

Figure 2. Same as **Fig. 1c** but for seasonal precipitation.

due to the large precipitation variability there. The northern branch of this pattern occurs in Dec.-Feb. (DJF(+1)) and Mar.-May (MAM(+1)) following the onset of an El Niño, and is not evident in the other two seasons (Fig. 2). On the other hand, the southern branch of the pattern exists in all seasons, although its position shifts northeastward from JJA(0) (Jun.-Aug. of an ENSO year) to MAM(+1) (Fig. 2).

Another new feature revealed by Figs. 1 and 2 is a coherent zonal band of precipitation anomalies (dry during El Niños) spanning the region from tropical America eastward all the way to tropical Africa. This band is evident in all seasons, but its position and width change seasonally. Associated with this tropical band, precipitation anomalies of opposite sign occur to the south and north extending to the subtropics across the Atlantic (mostly in DJF(+1) and MAM(+1)). During DJF(+1), the dry anomalies over tropical America are connected with the dry anomaly band in the North Pacific, while the wet anomalies over the subtropical Atlantic appear to be an extension of the anomalies over southern North America (Fig. 2).

During DJF(+1) and, to a smaller extent, MAM(+1), the wet anomaly (during El Niños) over the subtropical North Atlantic extends northeastward into Europe (Fig. 2), accompanied by anomalies of opposite sign to the south and north over the North Atlantic.

Over the tropical western Indian Ocean and adjacent eastern Africa, large precipitation anomalies with sign opposite to that to the east occur in SON(0) (Fig. 2). During MAM (+1), this anomaly pattern is confined to southern latitudes but extends to the tropical eastern Indian Ocean, while anomalies of opposite sign develop over adjacent southern Africa (also in DJF(+1)). This pattern is less evident in the other seasons.

Fig. 2 also shows relatively small-scale features over East Asia and the Indian sub-continent. ENSO precipitation anomalies have not been identified in these regions in previous analyses (e.g., *Ropelewski and Halpert*, 1987, 1989; X-A). During DJF(+1) of a strong-El Niño year, precipitation is ~30-80 mm (~100% of the mean precipitation) above normal over southeastern China and the East and South China Seas, while it is ~30-80 mm or 80-100% below normal over the region encompassing the Indian-subcontinent, central China, and Southeast Asia. The dry anomalies over India and central China are shifted southward during MAM(+1). Anomalies over Asia are small in the other seasons.

Precipitation anomalies switch sign during cold ENSO episodes (negative Darwin SLP anomalies). The precipitation amplitudes have been slightly larger during cold events than during warm events during the last five decades (Fig. 1a).

The ENSO EOFs explain about 4.5–7.0% (smallest in MAM(+1) and largest in SON(0)) of the total variance of *global* precipitation. During a typical El Niño year, the global mean precipitation is only ~2 mm/yr (0.2%) above normal, mainly because most of the anomalies result from shifts of rain-belts. Over many tropical areas (Indonesia-Australia, the equatorial Pacific and Atlantic), however, ~30–60% of the annual precipitation variance is explained by the ENSO mode, as implied by the correlation coefficients (Fig. 1b). Over the contiguous United States except

for the Northeast and Northwest, ENSO accounts for about 20–30% of the total variance of annual precipitation.

4. Discussion

The ENSO-induced precipitation anomaly maps presented here show many important new features and confirm those obtained previously. In the east-west direction, the anomaly patterns in the tropics result from changes in the Walker circulation during ENSO events. During warm ENSO episodes, ascending motion weakens over South America and subsidence over the Atlantic increases; while ascending motion over the equatorial western Indian Ocean and eastern Africa strengthens (*Webster and Chang*, 1988). Over the tropical eastern Pacific, the ITCZ moves equatorward during warm ENSO episodes (*Rasmusson and Carpenter*, 1982). This ITCZ shift reduces precipitation by about 100 mm/yr along the northern edge of the normal ITCZ over the eastern Pacific, mostly in DJF(+1) and MAM(+1) (Figs. 1c and 2).

Over the Indonesia region and east into the subtropical Pacific, the EOF patterns are consistent with enhanced subtropical divergence and a weakened east-Asia winter monsoon in the Northern Hemisphere, and with a weakened convergence zone east of Australia in the Southern Hemisphere (*Rasmusson and Carpenter* 1982). The latter results from a northeastward shift of the South Pacific Convergence Zone (SPCZ) during El Niños (*Rasmusson and Carpenter*, 1982; *Trenberth and Shea*, 1987). The SPCZ shift also contributes to the above-normal precipitation south of the equator over the central Pacific.

The extended range of the pattern from Indonesia to the subtropics clearly suggests that weakened moist convection over the western equatorial Pacific (and, probably, enhanced convergence over the central equatorial Pacific) is connected with atmospheric circulation anomalies over the subtropical Pacific through the Hadley cell (the trade winds at the surface) (*Trenberth et al.*, 1998). However, detailed analyses of atmospheric circulation anomalies that lead to the precipitation patterns over the entire Pacific are not available.

Some of the ENSO-associated extratropical precipitation anomalies we observe here have been related to large-scale atmospheric circulation changes caused by tropical sea surface temperature and wind anomalies. For example, the DJF(+1) ENSO precipitation anomalies over Canada can be explained by the associated upper-atmospheric flow patterns, which resemble the positive (negative) phase of the Pacific-North America (PNA) pattern during the first winter following the onset of El Niño (La Niña) events (*Shabbar et al.*, 1997). However, physical connections between the tropical ENSO anomalies and many other extratropical ENSO precipitation anomalies (e.g., over the North Atlantic and Europe during DJF(+1)) have not yet been established. In particular, the southeastward orientation of the ENSO precipitation anomalies over the South Indian and South Pacific Oceans (Fig. 2) seems to suggest that the Hadley cell (trade winds at the surface) is instrumental in generating the extratropical precipitation anomalies.

The patterns shown in Figs. 1 and 2 represent only the climatological mean. Individual ENSO events may vary substantially from the mean patterns. In addition, there may be low-frequency variations in the strength of the ENSO-precipitation relationships (*Power et al.*, 1999). Nevertheless, Figs. 1 and 2 may be used to forecast seasonal precipitation anomalies associated with an upcoming ENSO event over many regions, especially in the tropics.

Acknowledgments. This work was partly supported by the ACACIA Consortium and the NOAA Office of Global Programs (grant no. NA87GP0105). NCAR is sponsored by the National Science Foundation.

References

Dai, A., T.M.L Wigley, B. A. Boville, J.T. Kiehl, and L.E. Buja, Climates of the 20th and 21st centuries simulated by NCAR coupled system model. *J. Clim.*, submitted, 2000.

Dai, A., I. Y. Fung, and A. D. Del Genio, Surface observed global land precipitation variations during 1900-1988. *J. Clim.* **10**, 2943-2962, 1997.

Kiladis, G. N. and H. F. Diaz, Global climate anomalies associated with extremes in the Southern Oscillation. *J. Clim.* **2**, 1069-1090, 1989.

New, M., M. Hulme and P. Jones, Representing twentieth century space-time climate variability. II: Development of 1901-1996 monthly grids of terrestrial surface climate. *J. Clim.*, in press, 1999.

Power, S., T. Casey, C. Folland, A. Colman, and V. Mehta, Inter-decadal modulation of the impact of ENSO on Australia. *Clim. Dyn.*, **15**, 319-324, 1999.

Rasmusson, E. M. and T. H. Carpenter, Variations in tropical sea surface temperature and surface wind fields associated with the Southern Oscillation/El Niño. *Mon. Wea. Rev.* **110**, 354-384, 1982.

Ropelewski, C. F. and M.S. Halpert, Global and regional scale precipitation patterns associated with the El Niño/Southern Oscillation. *Mon. Wea. Rev.* **115**, 1606-1626, 1987.

Ropelewski, C. F. and M.S. Halpert, Precipitation patterns associated with the high index phase of the Southern Oscillation, *J. Clim.* **2**, 268-284, 1989.

Shabbar, A., B. Bonsal, and M. Khandekar, Canadian precipitation patterns associated with the Southern Oscillation. *J. Clim.* **10**, 3016-3027, 1997.

Trenberth, K. E. and D. J. Shea, On the evolution of the Southern Oscillation. *Mon. Wea. Rev.* **115**, 3078-3096, 1987.

Trenberth, K. E., G. W. Branstator, D. Karoly, A. Kumar, N.-C. Lau, and C. F. Ropelewski, 1998: Progress during TOGA in understanding and modeling global teleconnections associated with tropical sea surface temperatures. *J. Geophys. Res.* **103**, 14,291-14,324.

Webster, P. J. and H.-R. Chang, Equatorial energy accumulation and emanation regions: impacts of a zonally varying basic state. *J. Atmos. Sci.* **45**, 803-829, 1988.

Xie P. and P. A. Arkin, Global precipitation: a 17-year monthly analysis based on gauge observations, satellite estimates and numerical model outputs. *Bull. Am. Met. Soc.* **78**, 2539-2558, 1997.

A. Dai and T. M. L. Wigley, National Center for Atmospheric Research, P.O. Box 3000, Boulder, CO 80307. (e-mail: adai@ucar.edu)

(Received October 18, 1999; revised January 21, 2000; accepted February 22, 2000.)